An Analytical Framework for Rapid Estimate of Rain Rate during Tropical Cyclones

Reda Snaiki, Teng Wu*

Department of Civil, Structural and Environmental Engineering, University at Buffalo, State University of New York, Buffalo, NY 14126, USA

Corresponding author. Email: tengwu@buffalo.edu

Abstract: An analytical framework for rapid estimate of rain rate during a translating tropical cyclone was proposed in this study. The efficient analysis framework for rain field is based on the observation that rain-induced momentum flux at Earth's surface cannot be ignored. The total surface stress results mainly from momentum flux contributions of wind and rain. A height-resolving wind field was utilized during the model construction leading to a linear, analytical solution of the surface rain rate. The obtained rain rate model explicitly depends on parameters for a typical tropical cyclone wind field simulation, namely storm location, approach angle, translation speed, radius of maximum wind, pressure profile, surface drag coefficient, and turbulent diffusivity. Hence, it could be readily implemented into state-of-the-art tropical cyclone risk assessment using the Monte Carlo technique. The rainbands in the proposed methodology were simulated using a local perturbation scheme. Sensitivity analysis of the rainfall field to the abovementioned parameters was comprehensively conducted. The results generated by the present analytical framework for rapid estimate of rain rate during tropical cyclones are consistent with field measurements.

Keywords: Tropical cyclone, rain rate, wind field simulation, rain-induced stress.

1. Introduction

Tropical cyclones are responsible for the substantial part of natural hazard-induced economic and life losses through high winds, torrential rain and wind-driven storm surge. Among these, the rainfall-induced inland flooding contributes to a significant portion of the tropical cyclone related damages (e.g., Landsea 2000; Rappaport 2000). Therefore, the rain field simulation inside the tropical cyclone has attracted interest of a number of researchers for a better rainfall hazard assessment. While there have been considerable advances in improving the simulation accuracy of tropical cyclone rain field based on high-fidelity numerical weather prediction models, they are not practical for risk assessment due to their high computational demands. Usually, the rainfall distribution can be efficiently characterized based on probabilistic, parametric or physically-based schemes.

The probabilistic models give good insights on the exceedance rate of specific rainfall intensities, and are often used to predict the extreme rain rates. The development of this type of models usually suffer from a lack of a large number of historical data that are needed to fit the selected distributions. In addition, they are generally unable to represent the most important physics governing the rain field inside the tropical cyclone (e.g., sea surface temperature, moisture distribution, vertical wind shear, hurricane intensity and translational velocity). Actually, no physical justification has been provided for the use of the popular distributions such as lognormal, mixed-exponential and Gamma curves to fit the data (e.g., Woolhiser and Roldan 1982; Groisman et al. 1999; Wilson and Toumi 2005).

The construction of the parametric models also requires a huge amount of rain field measurements. Recently, the Tropical Rainfall Measuring Mission (TRMM) (Huffman et al.,

45 2010), a joint satellite mission of the National Aeronautics and Space Administration (NASA) and
46 the Japan Aerospace Exploration Agency (JAXA), has released a significant amount of tropical
47 cyclone rainfall data. The goal of TRMM is to provide good estimates of global precipitation using
48 satellite observations. TRMM contains several instruments, namely the TRMM Microwave
49 Imager (TMI), the Precipitation Radar (PR), the Visible Infrared Scanner (VIRS), the Lightning
50 Imaging Sensor (LIS), and the Clouds and Earth's Radiant Energy System (CERES). Details of the
51 TRMM instruments are given in Kummerow et al. (1998). Several empirical models have been
52 developed based on the TRMM database. For example, Lonfat et al. (2004) acquired the spatial
53 distribution of the rain field over the ocean using the TMI data from 1998 to 2000. The rain rates
54 were found to be heavily dependent on the sustained surface wind speed. The rain rate achieved
55 the maximum value near the radius of maximum winds and then decayed exponentially. According
56 to the hurricane intensities grouped into three categories, i.e., tropical storms, category 1-2 tropical
57 cyclones, and category 3-5 tropical cyclones, different radial variations of the rain rate were
58 obtained. Based on the findings from Lonfat et al. (2004) together with the surface rain gauge data,
59 Tuleya et al. (2007) proposed the Rainfall Climatology and Persistence (R-CLIPER) model. In this
60 parametric model, the rain rate presented a Rankine-like profile with a linear variation from the
61 tropical cyclone center to the radius of maximum rain rate, followed by an exponential decay. In
62 addition, it has been proved using the findings of Kaplan and DeMaria (1995) that the hurricane
63 rain rates and wind speeds are always highly correlated before/after landfall. While the R-CLIPER
64 model could be employed over both the ocean and land, it assumed a symmetric distribution of the
65 rain rate inside the tropical cyclone. Lonfat et al. (2007) improved the spatial variation of the rain
66 field by introducing a modified version of the R-CLIPER model known as the Parametric
67 Hurricane Rainfall Model (PHRaM) with consideration of the wind shear effects. However, both

68 the R-CLIPER and PHRaM models were found to underestimate the maximum rain rate since they
69 are based on the ensemble averages of numerous hurricanes (Tuleya et al. 2007).

70 Very few physics-based rain rate models have been introduced in the technical literature.
71 In the theoretical model proposed by Langousis and Veneziano (2009a), it is assumed that all the
72 upward moisture flux at the top of the tropical cyclone boundary layer is converted into rainfall.
73 The vertical moisture flux was evaluated from the vertical winds at a reference height, generated
74 by a modified version of the wind field model proposed by Smith (1968), along with the depth-
75 averaged temperature and saturation ratio. Although observations from Hurricane Frances
76 presented a maximum correlation (around 0.85) between the surface rain and vertical wind at an
77 elevation of 2-3 km, more comprehensive data may be necessary for the selected reference height.
78 Also, it is not easy to implement the modified version of Smith's non-linear model in the Monte
79 Carlo technique with a large number of simulations needed. While the model by Langousis and
80 Veneziano (2009a) has been demonstrated to provide good estimates of the tropical cyclone rain
81 rate, it cannot account for post landfall scenarios.

82 In this study, a new, analytical framework for tropical cyclones rain rate estimate will be
83 developed for high-efficiency simulations. The rain rate analysis framework is based on the
84 observation that rain-induced momentum flux at Earth's surface cannot be ignored (e.g., Caldwell
85 and Elliot 1971; 1972; Zhao et al. 2013). The total surface stress results mainly from momentum
86 flux contributions of wind and rain. A general formula of the rain intensity has been first derived
87 in which the iteration approach was utilized in the computation. The proposed methodology is able
88 to effectively integrate an efficient wind field model for rapid estimation of rain intensity during
89 tropical cyclones. Specifically, a height-resolving scheme recently developed by Snaiki and Wu
90 (2017a; 2017b) was utilized leading to a linear, analytical solution of the surface rain rate. The

rainbands in the proposed methodology were simulated using a local perturbation scheme (e.g., Samsury and Zipser 1995; Holland et al. 2010; Li and Wang 2012). Sensitivity analysis of the rainfall field to several essential parameters in the rain rate simulation was comprehensively conducted. The present analytical framework for rapid rain rate estimation has been validated using observation data obtained from various hurricanes.

2. An analytical framework for rain rate estimation

The heat and moisture fluxes that are considered as the fuel and the surface stress contributing to the dissipation essentially govern the intensity of a tropical cyclone (Chen et al. 2007), as illustrated in Fig. 1.

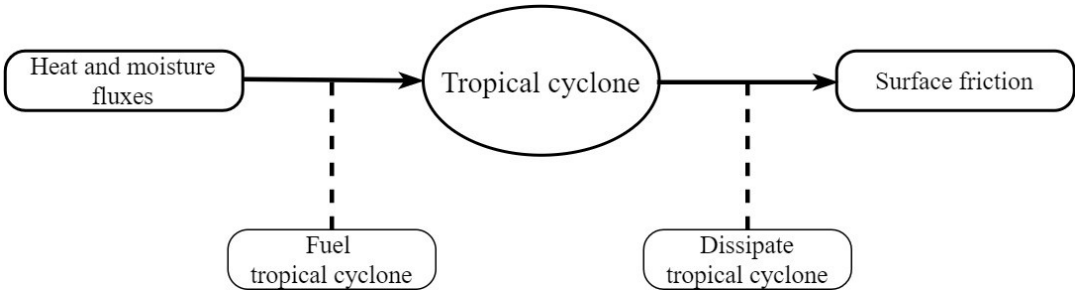

Fig. 1. Major processes governing tropical cyclone intensity

In this study, the modeling of rain intensity is based on the dissipation process of tropical cyclones where the total momentum flux is decomposed into several stress contributions. The general practice to consider the total surface shear stress or equivalently the momentum flux density τ is based on the following parameterization (Andreas 2004; Donelan et al. 2004; Jarosz et al. 2007; Huang 2012):

$$\tau \equiv \rho_a u_*^{2}{}_{effective} \quad (1)$$

where $u_{*effective}$ = effective frictional velocity during rain; and ρ_a = air density. This parameterization has been used in a number of applications such as the Fifth-generation Pennsylvania State University–National Center for Atmospheric Research Mesoscale Model (MM5) and the fully coupled atmosphere–wave–ocean model (AWO) (e.g., Chen et al. 2013). Furthermore, the effective frictional velocity can be related to the effective drag coefficient $C_{d,effective}$ and the wind speed V_{wind} based on the following formula:

$$u_{*\,effective}^{2} = C_{d,effective} V_{wind}^{2} \tag{2}$$

Therefore, the total shear stress can be expressed as:

$$\tau \equiv \rho_a C_{d,effective} V_{wind}^{2} \tag{3}$$

The square law as indicated in Eq. (3) has been comprehensively validated, especially at high wind speeds, with a number of observations (Garratt 1977).

Various factors may contribute to the total surface stress, namely the turbulent fluxes, rain effects, spray, airborne sediment (Saltation theory) and convection-induced stress. It is assumed here that no airborne sediment exists, therefore its momentum flux contribution is disregarded as well as the convection-induced stress (Huang 2012). The spray actually does not add extra momentum to the system but redistributes the wind stress near the surface (Andreas 2004). Since the droplets around the spray evaporate quickly (Emanuel 1995), its contribution is typically negligible (e.g., Wu 1973; Fairall et al. 1994). On the other hand, the rain-induced momentum flux can be significant as the raindrops interact with the near-surface wind and transfer momentum to the surface (Caldwell and Elliot 1971; 1972). Zhao et al. (2013) compared the rain-induced horizontal stress and the wind stress at various wind speeds and rain rates. It was demonstrated

that the horizontal stress by rain can have the same order of magnitude with that by wind. Therefore, it is important to consider the rain-induced stress contribution to the total stress near the surface. The total stress is then partitioned between two momentum contributions as:

$$\tau = \tau_a + \tau_r \tag{4}$$

where τ_a = momentum flux contribution from wind; and τ_r = momentum flux contribution from rain. The wind stress τ_a can be expressed, in a similar way as in Eq. (3), in terms of the drag coefficient C_d without rain effects:

$$\tau_a \equiv \rho_a C_d V_{wind}^2 \tag{5}$$

A widely used parametrization of the rain stress relates it to the rain rate and wind speed as (Caldwell and Elliott 1971; 1972):

$$\tau_r \equiv \gamma_r \rho_r V_{wind} R \tag{6}$$

where ρ_r = density of rainwater; γ_r = empirically determined factor varying between 0.8 and 0.9; and R = rain rate. In this study $\gamma_r = 0.85$ will be adopted (Caldwell and Elliott 1971; Wong and Toumi 2016). The parameterization of Eq. (6) has been incorporated in several models, e.g., the one-dimensional mixed-layer model developed by Clayson and Kantha (1999), the bulk parametrization outlined by Fairall et al. (1996), and the Regional Ocean Modelling System (ROMS). Equations (3), (4), (5) and (6) lead to the following formula of the rain rate:

$$R = \frac{\rho_a C_{d,effective} V_{wind}^2 - \rho_a C_d V_{wind}^2}{\gamma_r \rho_r V_{wind}} \tag{7}$$

It is interesting to note that the obtained rain rate formula implies that the rain-induced stress is proportional to the wind-induced one. The wind stress is well known to be responsible to maintain

150 the observed wind velocity profile in the atmospheric boundary layer (Taylor 1916). Since the
151 wind and rain horizontal velocities are proportional to each other (e.g., Guo et al. 2001; Fu et al.
152 2015), the relation between wind and rain-induced stresses indicated in Eq. (7) is reasonable. The
153 effective drag can be related to the roughness length based on the logarithmic law of wind profile
154 in the vicinity of the surface as (Meng et al. 1995; Bryant and Akbar 2016):

155 $$C_{d,effective} = \frac{\kappa^2}{\left[\ln\left(\frac{z_{10}}{z_{0,effective}}\right)\right]^2} \tag{8}$$

156 where $\kappa =$ von Karman coefficient; $z_{0,effective} =$ the effective roughness length; and $z_{10} = 10\,m$.
157 Similarly, the drag coefficient C_d (no rain effects) can be expressed in terms of the roughness
158 length z_0 as $C_d = \kappa^2 \Big/ \left[\ln\left(\frac{z_{10}}{z_0}\right)\right]^2$.

159 The studies of characterizing the rain-induced roughness length over land are very limited.
160 On the other hand, the logarithmic profile well representing the lower part of the boundary-layer
161 winds over both the ocean and land as indicate by a large number of field measurements (e.g.,
162 Powell et al. 2003; Vickery et al. 2009; Tse et al. 2013, Shu et al. 2017) provides a good approach
163 for the estimation of the effective frictional velocity. As a result, the effective drag coefficient
164 $C_{d,effective}$ may be obtained through the least squares fit of the measured or simulated (considering
165 rain effects) vertical wind speed profile in the linear logarithmic space (e.g., Powell et al. 2003;
166 Holthuijsen et al. 2012; Vickery et al. 2009; Bell et al. 2012). In this study, the height-resolving,
167 wind-rain interaction model developed by Snaiki and Wu (2017c) (see Appendix A) is utilized.
168 Since the rain rate is a necessary input to take the rain effects into account, the iteration technique
169 is employed in the simulation as illustrated by Fig. 2.

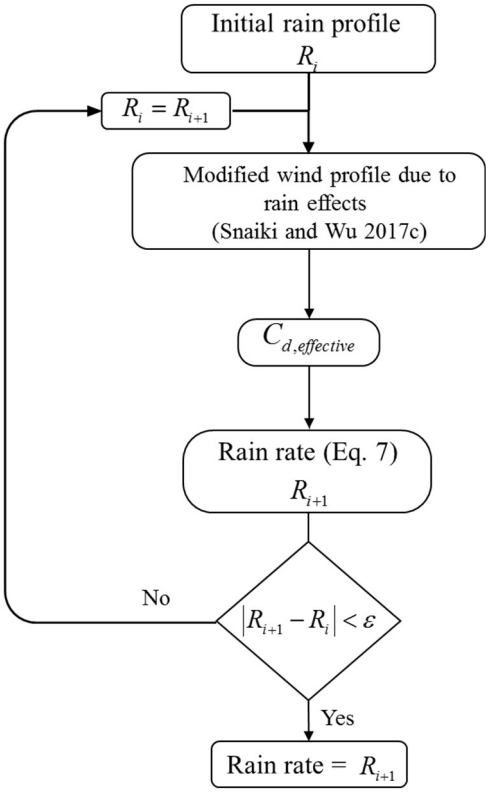

Fig. 2. Flow chart of the rain intensity simulation methodology

The initial guess of the rain profile could be based on an empirical model as follows (Snaiki and Wu 2017c):

$$R = R_{rm}\left\{\left(\frac{r_m}{r}\right)^b \exp\left[1-\left(\frac{r_m}{r}\right)^b\right]\right\}^{0.5} \tag{9}$$

where R_{rm} = maximum rain rate located at the radius of maximum wind r_m ; r = radial distance from the tropical cyclone center; and b = scaling parameter that adjusts the profile shape and depends on the radial extent of the tropical cyclone rain field. The maximum rain rate R_{rm} was estimated with an empirical formula available in literature (Tuleya et al. 2007):

$$R_{rm} = a + b\left[1+\left(V_m - 35\right)/33\right] \tag{10}$$

where a and b = constants from the least squares fit of the TRMM radial rainfall rates; and V_m = maximum wind speed. Although the iterative calculation is required in the analysis, it converges quite rapidly. With a good initial guess of the rain profile based on Eq. (9), two or three iterations are needed with a prescribed threshold ε= 5% for all simulations in the present study. The first-order closure of the rain rate simulation in Fig. 2 results in a simplified model of Eq. (7):

$$R = \frac{\rho_a k_m \frac{dV_{wind,modified}}{dz} - \rho_a k_m \frac{dV_{wind}}{dz}}{\gamma_r \rho_r V_{wind}} \tag{11}$$

where $k_m = 100\ m^2/s$ is the eddy viscosity; $V_{wind,modified}$ = modified wind speed due to the rain effects.

In the case of the marine conditions, the effective roughness length $z_{0,effective}$ could be expressed as a combination of the aerodynamic roughness length z_0 and the rain-induced one $z_{0,r}$ (Kumar et al. 2009):

$$z_{0,effective} = z_0 + z_{o,r} \tag{12}$$

Several formulas have been proposed in the literature to characterize the rain-induced roughness length $z_{0,r}$ over ocean. For instance, Kitaigorodskii [referred in Houk and Green (1976)] defined $z_{0,r}$ as:

$$z_{o,r} = 0.03\sigma \tag{13}$$

where σ is the standard deviation of the experimentally obtained mean water level:

$$\sigma = \beta \frac{kD}{g\upsilon} \tag{14}$$

where β = a constant of 0.01; D = drop diameter; g = gravitational acceleration; υ = kinematic viscosity of water; and k is the rain kinetic energy flux that can be related to the rain intensity R and the terminal velocity of the rain drop V_t:

$$k = \frac{RV_t^2}{2} \tag{15}$$

As a result, the rain-induced roughness can be expressed as:

$$z_{0,r} = \frac{0.015\beta D V_t^2 R}{g\upsilon} \tag{16}$$

Accordingly, the rain rate over ocean can be calculated as:

$$R = \frac{\rho_a \kappa^2 V_{wind} \left(\left[\ln\left(\frac{z_{10}}{z_0 + z_{0,r}} \right) \right]^{-2} - \left[\ln\left(\frac{z_{10}}{z_0} \right) \right]^{-2} \right)}{\gamma_r \rho_r} \tag{17}$$

It should be noted that the use of Eq. (17) requires an iteration process since the rain-induced roughness length $z_{0,r}$ depends on the rain intensity.

3. Wind field model

The proposed analytical framework for rapid estimate of the rain rate requires the horizontal wind speed components as input. A recently developed height-resolving model by Snaiki and Wu (2017a; 2017b) is utilized here due to its high efficiency to obtain the wind field. A brief discussion of the wind field model is presented in this section for the sake of completeness. The governing equation of the wind field is described as follows:

$$\frac{\partial \boldsymbol{v}}{\partial t} + \boldsymbol{v}.\nabla \boldsymbol{v} = -\frac{1}{\rho_a}\nabla p - f\boldsymbol{k} \times \boldsymbol{v} + \boldsymbol{F} \tag{18}$$

where f = Coriolis parameter; p = pressure; $\boldsymbol{k}$ = unit vector in the vertical direction; and $\boldsymbol{F}$ = frictional force. In order to solve Eq. (18), the decomposition method is used where the wind velocity ($\boldsymbol{v}$) is expressed as:

$$\boldsymbol{v} = \boldsymbol{v_g} + \boldsymbol{v'} \tag{19}$$

where $\boldsymbol{v_g}$ = gradient wind in the free atmosphere; and $\boldsymbol{v'}$ = frictional component near the ground surface. The solution of the gradient wind speed could be solved straightforwardly in the cylindrical coordinate system (Georgiou 1986; Meng et al. 1995):

$$v_{\theta g} = \frac{\left(-csin\left(\theta - \upsilon\right) - fr\right)}{2} + \left[\frac{\left(-csin\left(\theta - \upsilon\right) - fr\right)^2}{4} + \frac{r}{\rho_a}\frac{\partial p}{\partial r}\right]^{1/2} \tag{20}$$

where υ = approach angle (counter clockwise positive from the East); c = translation speed of the tropical cyclone; and θ = azimuthal angle. The radial velocity $v_{rg} = -\frac{1}{r}\int_0^r \frac{\partial v_{\theta g}}{\partial \theta} dr$ obtained from the continuity equation is usually disregarded due to its insignificant effects (Meng et al. 1995).

To obtain the frictional wind speed component, the nonlinear governing equation is first simplified using the scale analysis approach, and then linearized leading to the following frictional wind speed formulas as:

$$u'(\theta, z') = \left(\alpha/\beta\right)^{1/2} \times Real\left\{A_0 \times e^{(q_0 z')} + A_1 \times e^{(q_1 z' + i\theta)} + A_{-1} \times e^{(q_{-1} z' - i\theta)}\right\} \tag{21a}$$

$$v'(\theta, z') = Imag\left\{A_0 \times e^{(q_0 z')} + A_1 \times e^{(q_1 z' + i\theta)} + A_{-1} \times e^{(q_{-1} z' - i\theta)}\right\} \tag{21b}$$

where (u', v') = frictional components of the wind velocity; $q_1 = -(1+i)\left[\gamma + \sqrt{\alpha\beta} - \phi\right]^{1/2}$; $q_{-1} = -(1+i)\left[-\gamma + \sqrt{\alpha\beta} - \phi\right]^{1/2}$; $q_0 = -(\alpha\beta)^{1/4}$; $\alpha = \frac{1}{2k_m}\xi_g$; $\beta = \frac{1}{2k_m}\xi_{ag}$; $\xi_g = \frac{2v_{\theta g}}{r} + f$ is the absolute angular velocity; $\xi_{ag} = \frac{\partial v_{\theta g}}{\partial r} + \frac{v_{\theta g}}{r} + f$ is the vertical component of absolute vorticity of the gradient wind; $\gamma = \frac{1}{2K}\frac{v_{\theta g}}{r}$; $\phi = \frac{1}{2Kr}\frac{\partial v_{\theta g}}{\partial \theta}$; and *z'*= new vertical coordinate used as the base of the computation scheme where *z'*=0 is located above z_{10} (i.e., the 10 m height above the mean height of roughness elements) (Meng et al. 1995). The other necessary parameters needed for the simulation can be acquired in Snaiki and Wu (2017a; 2017b).

4. Model validation

The necessary parameters needed for the tropical cyclone wind field simulation are: υ approach angle; *c* translation velocity of the hurricane; p_c central pressure; Δp central pressure difference; $R_{\max}$ radius of maximum winds; *B* Holland's parameter; ψ latitude; and λ longitude. These wind parameters can be obtained from the National Hurricane Center's North Atlantic Hurricane Database (HURDAT). On the other hand, the tropical cyclone rainfall data can be acquired from the high-fidelity numerical weather prediction models, the Tropical Rainfall Measuring Mission (TRMM) database or the Radar observations.

4.1. Comparison with MM5 model

In this section, the ensemble average of 12 surface rain fields corresponding to hurricane Frances (2004) in the period from 29th August to 1st September 2004 (6-h intervals) were simulated based

on the Fifth-Generation Pennsylvania State University/NCAR Mesoscale Model (MM5) (Langousis and Veneziano 2009a). A resolution of 1.67 km was used to generate the azimuthally averaged rain rates in the MM5 simulations. The rain rates obtained from MM5 were compared with those based on the proposed analytical framework, where the necessary parameters for the rain intensity simulation were extracted from the HURDAT database (Table 1). As shown in Fig.3, a good agreement between the MM5 and present simulation results is achieved.

Table 1. Tropical cyclones characteristics of the selected 12 rain fields

Mon|Day|h	Hurricane Center		Storm Speed (m/s)	Storm Direction (deg)	V_{max} (m/s)	Δp (hpa)	R_{max} (km)
	Latitude (deg)	Longitude (deg)					
08|29|00	18.1	-52.9	4.0	145	59.2	948	31
08|29|06	18.4	-53.6	3.8	156	59.2	948	31
08|29|12	18.6	-54.4	4.0	165	59.2	948	31
08|29|18	18.8	-55.0	3.5	161	56.6	948	31
08|30|00	18.9	-55.8	3.9	172	54.0	954	32
08|30|06	19.0	-56.8	4.9	174	51.4	958	33
08|30|12	19.2	-58.1	6.4	171	51.4	956	33
08|30|18	19.4	-59.3	5.9	170	56.6	948	31
08|31|00	19.6	-60.7	6.9	171	56.6	946	31
08|31|06	19.8	-62.1	6.9	171	59.2	950	32
08|31|12	20.0	-63.5	6.9	171	61.7	949	32
08|31|18	20.3	-65.0	7.4	168	64.3	942	30

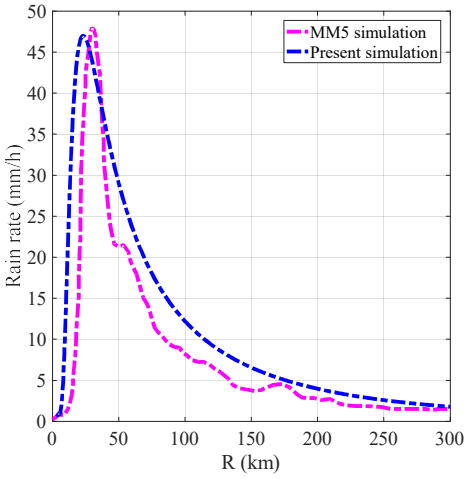

Fig. 3. Comparison of the azimuthally-averaged, rain-rate radial profile of Hurricane Frances

260 **4.2. Comparison with PR/TRMM rain fields**

261 To validate the proposed analysis framework for rapid rain rate estimation during tropical
262 cyclones, 38 PR/TRMM rain frames with a spatial resolution of $5\ km \times 5\ km$ were utilized. The
263 parameters of the data collected from the PR/TRMM rain frames are summarized in Table 2
264 (Langousis and Veneziano 2009b). These 38 frames were selected from eight tropical cyclones
265 that cover a wide range of storm intensities. Fig. 4(a) represents a scatterplot of the ratios between
266 the PR/TRMM and simulated rain intensities i_{PR} / i_{sim}. A total number of 73819 points were
267 selected from the 38 TRMM frames, covering a wide range of tropical cyclone spatial locations.
268 All the necessary parameters for the rain rate simulation are taken from Table 2 (Langousis and
269 Veneziano 2009b).

270 A large dispersion similar to the finding of Langousis and Veneziano (2009a) is observed in
271 Fig. 4(a). It mainly results from the significant small-scale variability of rain rate due to the
272 rainbands and local intensifications. Figure 4(b) depicts the local average and standard deviation
273 of the ratio i_{PR} / i_{sim} with a moving window of 2000 points. Clearly, the simulation based on the
274 proposed analyses framework of rain field is unbiased since the moving average is close to unity.
275 The moving standard deviation on the other hand is quite large highlighting the significance of the
276 small-scale variability of the tropical cyclone rain field (Powell 1990; Molinari et al. 1994;
277 Langousis and Veneziano 2009a).

278

279

280

281

282 **Table 2.** Tropical cyclones characteristics of the PR/TRMM rain fields (Langousis and Veneziano 2009b)

Hurricane Name	Hurricane Center Latitude (deg)	Hurricane Center Longitude (deg)	Storm Speed (m/s)	Storm Direction (deg)	V_{max} (m/s)	R_{max} (km)	TRMM Frame	Storm Intensity
Floyd 1999	21.7	-61.6	4.9	143	48.8	41	10290	CAT2
	23.5	-68.7	4.8	169	64.0	37	10317	CAT4
	23.7	-70.6	5.8	171	69.3	37	10321	CAT4
Lili 2002	23.6	-87.2	9.0	162	51.5	20	27826	CAT2
	24.4	-88.4	6.2	141	56.5	20	27830	CAT2
	28.4	-91.4	10.1	117	54.0	20	27842	CAT4
	29.0	-91.9	5.4	124	41.1	20	27845	CAT2
Frances 2004	12.6	-43.7	10.9	158	23.1	37	38646	TS
	15.7	-49.8	5.4	139	51.4	19	38667	CAT3
	17.0	-51.3	5.3	139	54.0	28	38677	CAT3
	17.9	-52.6	4.3	144	59.1	28	38682	CAT4
	19.0	-57.3	4.9	180	51.4	28	38708	CAT3
	21.2	-68.5	6.1	162	61.7	28	38739	CAT4
Ivan 2004	8.9	-38.9	7.6	184	25.7	37	38789	TS
	10.7	-50.6	12.2	185	57.5	28	38814	CAT4
	11.2	-53.4	8.1	173	51.4	28	38820	CAT3
	12.3	-64.1	8.3	166	61.7	19	38845	CAT4
	12.7	-66.2	7.3	164	61.7	20	38851	CAT4
	17.4	-77.3	4.1	194	66.8	28	38892	CAT4
	17.7	-78.4	4.4	153	64.3	28	38897	CAT4
	25.6	-87.4	5.5	112	61.7	46	38954	CAT4
Jeanne 2004	27.4	-70.6	5.5	0	38.6	42	39045	CAT1
	25.5	-69.5	1.1	207	41.1	37	39079	CAT2
	26.5	-74.3	7.4	173	43.7	60	39106	CAT2
	26.5	-75.6	6.5	180	46.3	46	39110	CAT2
Karl 2004	11.5	-35.3	7.1	176	26.7	37	38987	TS
	17.3	-45.5	2.0	166	57.8	32	39033	CAT3
	19.1	-47.4	5.9	121	64.0	32	39048	CAT4
	22.9	-48.6	8.2	112	54.0	28	39059	CAT3
	25.7	-49.5	6.8	117	48.8	28	39063	CAT3
Katrina 2005	24.6	-85.6	2.1	153	51.5	56	44357	CAT3
	25.0	-86.2	3.5	146	56.5	50	44361	CAT3
	26.9	-89.0	5.5	135	75.0	38	44373	CAT5
Rita 2005	24.3	-85.9	5.7	189	61.7	28	44743	CAT4
	24.9	-88.0	3.9	166	77.1	19	44754	CAT5
	25.4	-88.7	4.3	153	72.0	19	44758	CAT5
	26.8	-91.0	5.5	135	59.1	37	44770	CAT4
	27.4	-91.9	4.8	143	59.1	37	44773	CAT4

283

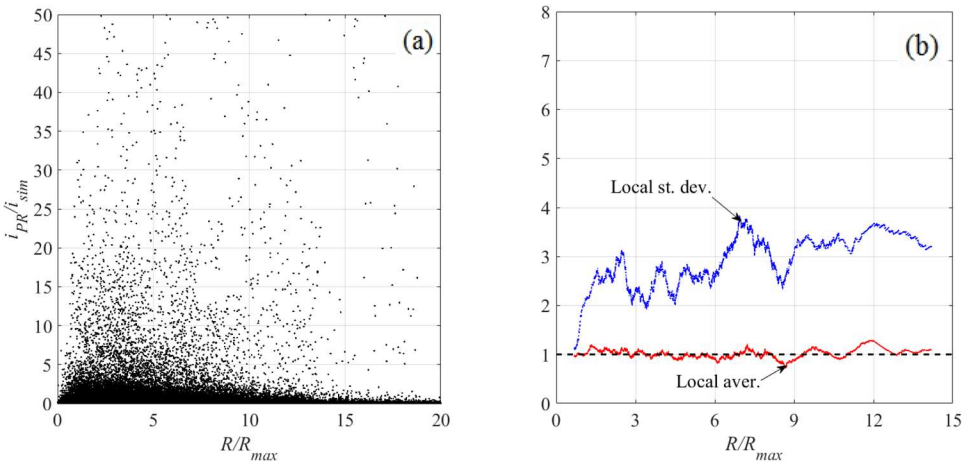

284

285 **Fig. 4.** Comparison of the PR/TRMM and simulated rain rates: (a) Scatter plot of i_{PR} / i_{sim}; (b) Local average and
286 standard deviation of i_{PR} / i_{sim}

287

288 **4.3. Comparison with TMI/TRMM and radar observations**

289 The rain distribution of hurricane Dennis (1999) obtained from TMI/TRMM (Lonfat et al. 2004)
290 was compared with the simulation result from the present methodology. As shown in Fig. 5, a
291 good agreement between the simulations and observations is highlighted except in some local
292 intensification regions caused by rainbands. TMI measurements are known to be more accurate
293 for rainfall estimates over ocean than land. On the other hand, the Hydro-Next-Generation Doppler
294 Radar system can measure the rainfall distribution over both ocean and land with very good
295 accuracy (Lin et al. 2010). Hurricane Isabel (2003) was employed here to validate rain field
296 simulation over land based on the present analysis framework. Isabel made landfall in North
297 Carolina on 18 September 2003 as a category 2 tropical cyclone and caused widespread damages
298 from storm surge flooding, wind and riverine flooding (Lin et al. 2010). Figure 6 presents a good
299 agreement between the simulated and observed rainfall distribution up to 200 km radius. The
300 orographic enhancement of rainfall due to the interaction between the tropical cyclone and the

complex terrain conditions of the central Appalachians Mountains, not considered in the present model, resulted in large differences beyond the range of 200 km (Lin et al. 2010).

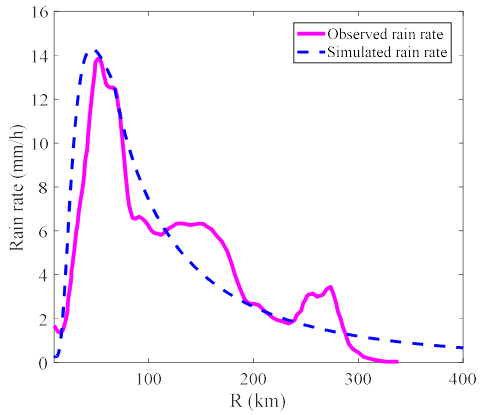

Fig. 5. Comparison of the azimuthally-averaged, rain-rate radial profile of Hurricane Dennis

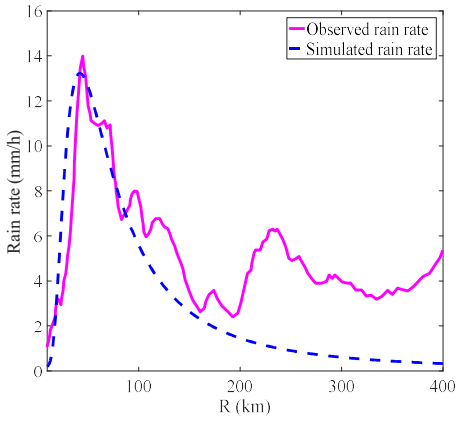

Fig. 6. Comparison of the azimuthally-averaged, rain-rate radial profile of Hurricane Isabel

5. Rainband simulation

Tropical cyclones exhibit significant rain rate in the eyewall and a set of rainbands (Willoughby et al. 1984; Willoughby 1988). The complicated underlying mechanisms governing the rainbands make their pattern vary from one tropical cyclone to another (Houze et al. 2006). Hence, it is extremely challenging to systematically simulate these rainbands. The rainbands outside the eyewall are usually characterized by secondary horizontal wind maxima (Samsury and Zipser

1995). A number of field measurements indicate that the local boundary-layer wind maxima in the rainbands are typically associated with pressure perturbations (e.g., Powell 1990; Yu and Tsai 2010; Lin et al. 2010; Sitkowski et al. 2011; Li and Wang 2012). Since the wind field here is simulated by a large-scale model (Snaiki and Wu 2017a; 2017b) and hence does not account for local intensifications, considerable differences between the simulated and observed rain rates are typically observed in the rainband regions as discussed in the preceding sections.

A good approach to improve the simulation would be based on a proper perturbation of the original wind profile that could characterize the rainbands. The rain rate heavily depends on the wind speed, hence, a perturbation in the wind field will generate a corresponding perturbation in the rain rate and hence the local maxima of the rain intensity (local perturbation scheme). This approach can be more convenient to be implemented by introducing a perturbation in the pressure profile that will generate a corresponding wind perturbation (Holland et al. 2010). To illustrate the adopted scheme, the rain field of hurricane Dennis (Fig. 5) was revisited to incorporate the contribution of the rainbands. The rainband locations were first identified from the TMI imagery [Fig. 7(b)]. Then, the simulated wind speeds at a 10-meter height were compared with those from the Remote Sensing System QuikScat (version-4) data [Fig. 7(a)] (Ricciardulli and Wentz, 2015) to obtain the perturbation values. Table 3 compares and presents the observed and simulated wind speeds in three different rainband regions. The consideration of perturbations in the wind field leads to an improved rain rate, as shown in Fig. 8. A good agreement between the observed and simulated profiles is observed. Figure 9 presents a comparison of the simulated rain rates of Hurricane Dennis with and without considerations of the rainbands. The corresponding correlation coefficients between the observations and simulations are 0.96 and 0.92, respectively. While the results demonstrate that the rain intensities predicted by both approaches match reasonably well

with the measured data, the simulation accuracy is certainly improved by integrating the rainband effects.

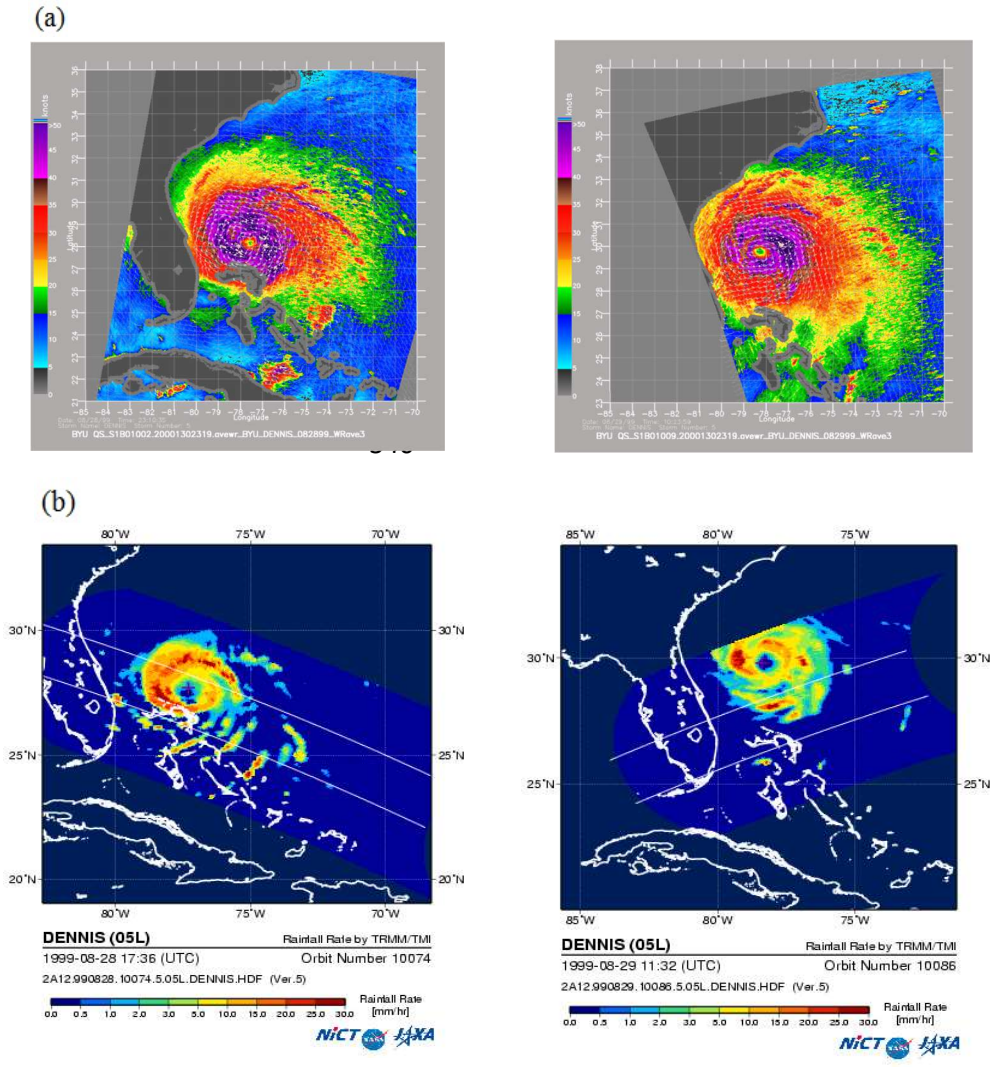

Fig. 7. Hurricane Dennis (1999) wind and rain fields: (a) Surface wind speed distribution obtained from QuikScat on August 28 (left) and August 29 (right); (b) Surface rain rate provided by TMI/TRMM on August 28 (left) and August 29 (right)

Table 3. Comparison between the observed (QuikScat) and simulated surface wind speed of Hurricane Dennis in the rainband regions

r (km)	θ (deg)	$U_{QuikScat}$ (m/s)	$U_{simulated}$ (m/s)
133	90	25.70	22.20
137	60	25.00	22.25
236	194	16.00	12.00

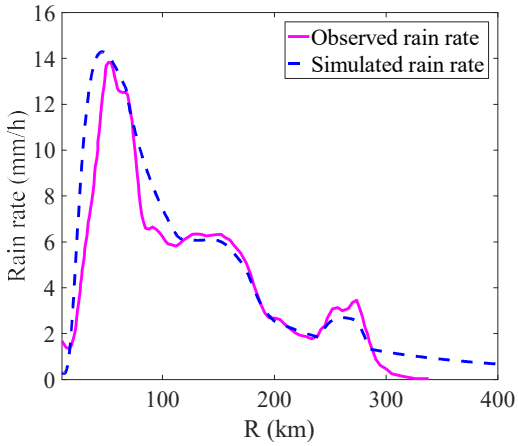

Fig. 8. Comparison of the improved, azimuthally-averaged, rain-rate radial profile of Hurricane Dennis

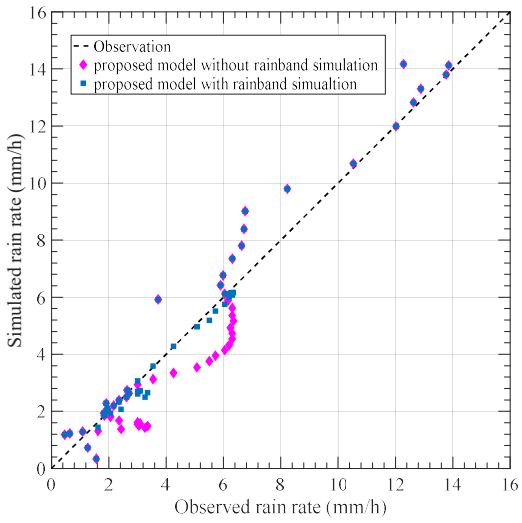

Fig. 9. Comparison of the azimuthally-averaged rain rates of Hurricane Dennis

6. Sensitivity analysis

Numerous studies have demonstrated based on field measurements and numerical simulations that the rainfall distribution varies with a number of environmental factors (e.g., roughness) and inherent tropical cyclone features (e.g., intensity and translation speed) (Lonfat et al, 2004). The present rain rate analysis framework explicitly depends on these parameters. Figure 10 illustrates the sensitivity of the rain intensity to several selected parameters, namely B Holland parameter, r_m radius of maximum wind, c translation speed, Δp central pressure difference, k_m turbulent diffusivity, and z_0 equivalent roughness length. The base case scenario is taken as: $B = 1$, $r_m = 30km$, $c = 10m/s$, $\Delta p = 70hpa$, $k_m = 50m^2/s$, and $z_0 = 0.001m$. The radial profile of the rain rate was taken at $\theta = 0°$ (counterclockwise positive from the East) for all simulations.

As indicated in Fig. 10, the central pressure difference Δp, translational tropical cyclone speed c and surface roughness z_0 have significant effects on the rain rate. Actually, it has been widely reported that the surface roughness can substantially alter the rain intensity (e.g., Trenberth et al. 2007; Langousis and Veneziano 2009a; and Lin et al. 2010). Also, a higher value of Δp, corresponding to a larger maximum wind v_m (Holland et al. 2010), leads to more intense rain. This result agrees with the observations and findings of the literature (e.g., Lonfat et al. 2004; Tuleya et al. 2007; Langousis and Veneziano 2009a). Similarly, an increase of the translational tropical cyclone speed results in the enhancement of the total precipitation. Figure 10 also implies that the smaller radius of maximum wind is associated with a more peaked profile shifted to the tropical cyclone center. The Holland's parameter *B* mainly modifies the decay rate of the rainfall intensity profile and presents small effects on the maximum rain rate. In addition, low sensitivity of the rain rate to the vertical turbulent diffusivity is noted in the figure.

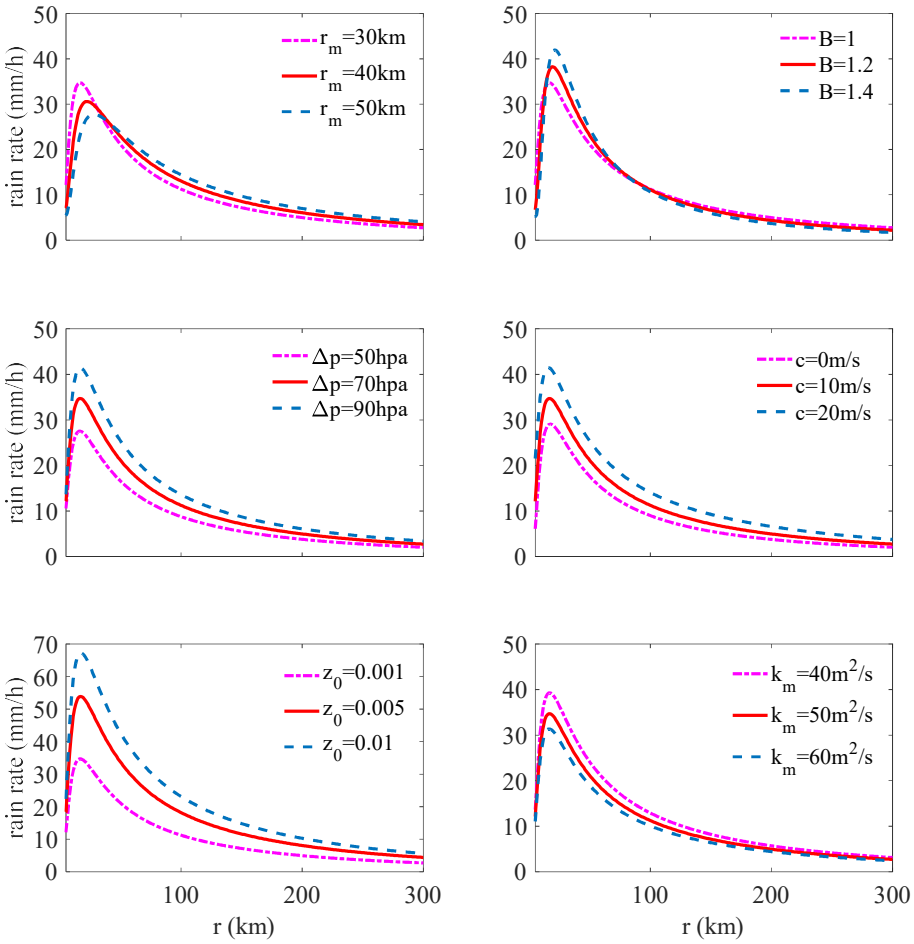

386

387 **Fig. 10.** Sensitivity analysis of the rain rate at $\theta = 0°$

388

389 The spatial distribution of the rain intensity was investigated based on the following case

390 study parameters: B = 1.2; c = 3 *m/s*; r_m = 40 *km*; Δp = 60 *hpa*; z_0 = 0.01*m*. Figures 11(a) and

391 11(b) depict the three-dimensional shaded surface of the rain intensity and their corresponding

392 contours, respectively. Due mainly to the tropical cyclone motion, the rain field is asymmetric.

393 This result conforms with the finding of Langousis and Veneziano (2009a), highlighting the

394 maximum rain rate location near the radius of maximum winds in the eyewall region (Lonfat et al.

395 2004; Tuleya et al. 2007).

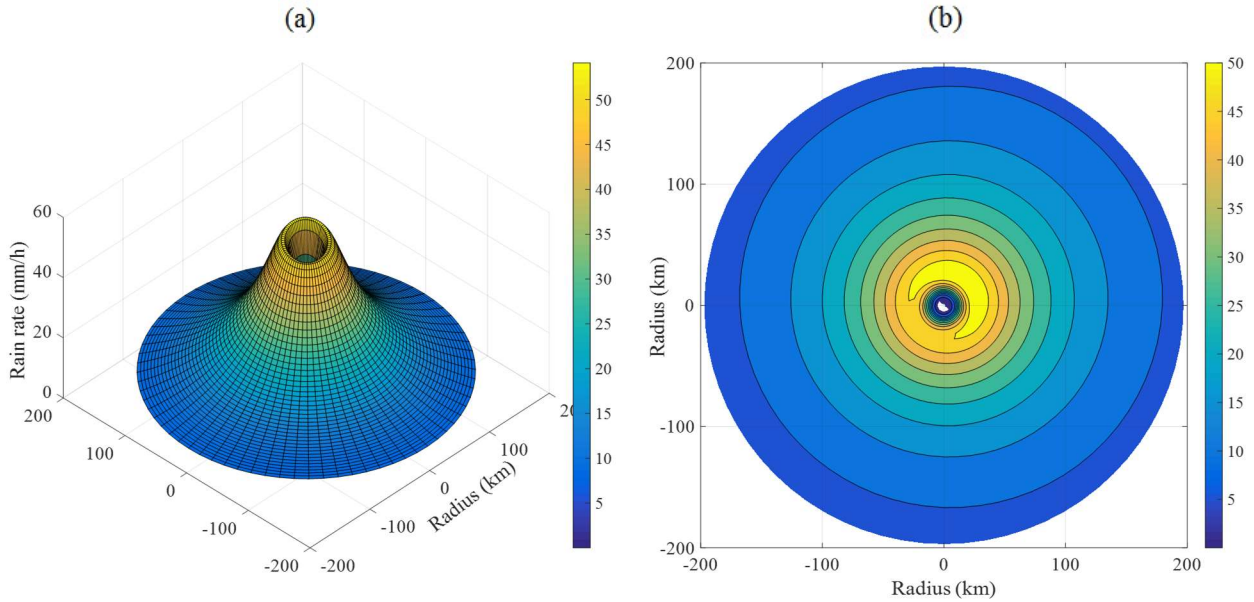

Fig. 11. Spatial distribution of the rain rate: (a) Three-dimensional shaded surface of the rain intensity; (b) Contours of the rain rate

7. Concluding remarks

A new, analytical framework for rapid rain rate estimation was proposed in this study. The rain rate formula was essentially developed based on the observation that rain-induced momentum flux at the surface cannot be ignored. The total surface stress results mainly from momentum flux contributions of wind and rain. The obtained results indicate that the spatial distribution of the rainfall field is governed by the wind field inside the tropical cyclone. This observation confirms the findings of several previous studies in which the rain intensity is shown to be highly correlated with the horizontal wind speed. A recently developed, height-resolving wind field model was utilized during the model construction leading to a linear, analytical solution of the surface rain rate. The obtained analysis framework for rain field explicitly depends on parameters for a typical tropical cyclone wind field simulation, namely storm location, approach angle, translation speed, radius of maximum wind, pressure profile, surface drag coefficient, and turbulent diffusivity. The

sensitivity analysis was extensively carried out to investigate the effects of several tropical cyclone and environmental parameters on the rain rate. It has been demonstrated that the rain rate heavily depends on the central pressure difference, translational tropical cyclone speed and surface roughness. The proposed analysis framework for the rain field is based on the large-scale horizontal wind field, therefore, it does not account for local rainfall intensifications due to rainbands. A plausible approach based on the local perturbation scheme was introduced to simulate the rain rates inside the rainband regions. The present analytical framework for rapid estimate of rain rate offers good simulation results that are consistent with tropical cyclone observations. It can be readily used in conjunction with the Monte Carlo techniques for risk analysis of tropical cyclone hazards.

Acknowledgments

The support for this project provided by the NSF Grant # CMMI 15-37431 is gratefully acknowledged.

Appendix A

The drag force f_i exerted by one raindrop on air in the horizontal direction is introduced:

$$\boldsymbol{f}_i = \frac{1}{2}\rho_a C_{d,r} V_{rel}(\boldsymbol{V}_{rain} - \boldsymbol{V}_{wind})\pi r_d{}^2 \tag{A.1}$$

where $C_{d,r}$ = drag coefficient for a raindrop of radius r_d; $\boldsymbol{V}_{rain}$ = raindrop horizontal velocity; $\boldsymbol{V}_{wind}$ = wind velocity in the horizontal direction; and V_{rel} = the total relative speed of the raindrop. As a result, the total drag force $\boldsymbol{f}_d$ applied on a tiny volume of air $V = A\Delta z$ can be obtained as follows:

$$\boldsymbol{f}_d = \frac{3R\rho_a C_{d,r} V(\boldsymbol{V}_{rain} - \boldsymbol{V}_{wind})}{4d} \tag{A.2}$$

where d = the raindrop diameter. The total drag force is then integrated into the governing equation of the wind velocity [Eq. (18)]. With several mathematical manipulations, one can obtain the gradient wind speed as follows (Snaiki and Wu 2017c):

$$v_{\theta g} = \frac{-\left(f + \frac{A^2}{\xi_{ag}}\right) + \frac{c\sin(\upsilon-\theta)}{r}\left(1 + \frac{A^2}{\xi_{ag}{}^2}\right)}{\frac{2}{r}\left(1 + \frac{A^2}{\xi_{ag}{}^2}\right)} + \frac{\left[\left(f + \frac{A^2}{\xi_{ag}} - \frac{c\sin(\upsilon-\theta)}{r}\left(1 + \frac{A^2}{\xi_{ag}{}^2}\right)\right)^2 + \frac{4}{\rho_a r}\frac{\partial p}{\partial r}\left(1 + \frac{A^2}{\xi_{ag}{}^2}\right)\right]^{1/2}}{\frac{2}{r}\left(1 + \frac{A^2}{\xi_{ag}{}^2}\right)} \tag{A.3}$$

where $A = \frac{\pi C_{d,r} N r_d{}^2}{2}\gamma_1$; and $N = \frac{3R}{4\pi r_d{}^3}$ is the number of raindrops per second on a unit area. On the other hand, the frictional wind speed components can be obtained as follows (Snaiki and Wu 2017c):

443 $$v_r' = Ye^{-az'}\left[W_1\cos(bz') + W_2\sin(bz')\right] \quad \text{(A.4a)}$$

444 $$v_\theta' = e^{-az'}\left[W_2\cos(bz') - W_1\sin(bz')\right] \quad \text{(A.4b)}$$

445 where $Y = \sqrt{p/q}$; $p = \frac{1}{2k_m}\xi_g$; $q = \frac{1}{2k_m}\xi_{ag}$; $A' = \frac{NC_{d,r}\pi r_d^{\,2}}{2}\gamma_2$. The variables *a* and *b* are defined

446 as:

447 $$a = \sqrt{\frac{A'/k_m + \sqrt{A'^2/k_m^{\,2} + 4pq}}{2}} \quad \text{(A.5a)}$$

448 $$b = \sqrt{\frac{\sqrt{A'^2/k_m^{\,2} + 4pq} - A'/k_m}{2}} \quad \text{(A.5b)}$$

449 The variables W_1 and W_2 are determined form the boundary conditions and presented as follows:

450 $$W_1 = -\frac{\left(a/b + \chi - Z\right)\left(\chi/Y - Z/Y\right)v_{rg} + \left(\chi - Z\right)v_{\theta g}}{1 + \left(\frac{a}{b} + \chi - Z\right)^2} \quad \text{(A.6a)}$$

451 $$W_2 = \frac{\left(\chi/Y - Z/Y\right)v_{rg} - \left(a/b + \chi - Z\right)\left(\chi - Z\right)v_{\theta g}}{1 + \left(a/b + \chi - Z\right)^2} \quad \text{(A.6b)}$$

452 where $\chi = \frac{C_{d,a}|v_s|}{kb}$; $Z = \frac{\gamma_r\rho_r R}{\rho_a bk}$; and $\boldsymbol{v_s}$ = total wind velocity near the ground surface.

453 Hurricane Katrina (2005) is employed here for the validation purpose. The anemometer

454 was located on the 42003 station at (26°0'25" N, 85°38'54" W). The 10-min averaged time was

455 used for the observed wind data at approximately 10 m height. As shown in Fig. 12, the results
456 generated by the present model are consistent with hurricane Katrina wind field observations.

457

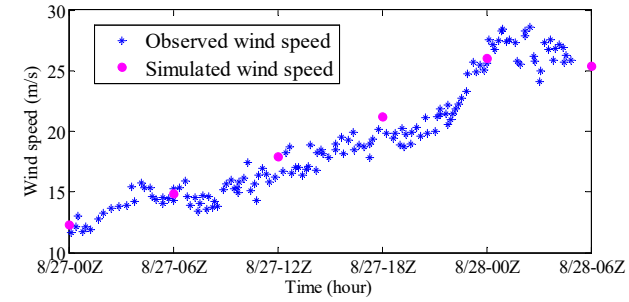

458

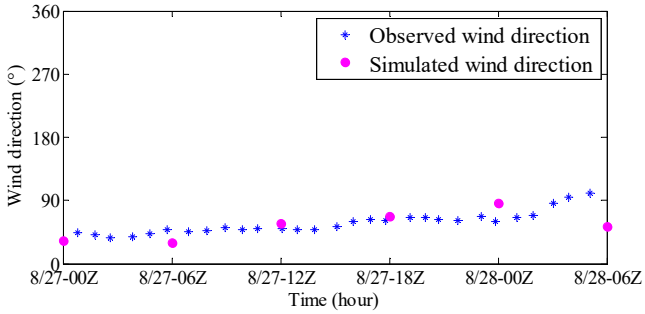

459 **Fig. 10.** Observed and simulated wind speeds (top) and directions (bottom) of Hurricane Katrina

460

461

References

Andreas, E.L., 2004. Spray stress revisited. Journal of Physical Oceanography, 34(6), pp.1429-1440.

Bryant, K.M. and Akbar, M., 2016. An Exploration of Wind Stress Calculation Techniques in Hurricane Storm Surge Modeling. Journal of Marine Science and Engineering, 4(3), 58.

Bell, M.M., Montgomery, M.T. and Emanuel, K.A., 2012. Air–sea enthalpy and momentum exchange at major hurricane wind speeds observed during CBLAST. Journal of the Atmospheric Sciences, 69(11), pp.3197-3222.

Caldwell, D.R. and Elliott, W.P., 1971. Surface stresses produced by rainfall. Journal of Physical Oceanography, 1(2), pp.145-148.

Caldwell, D.R. and Elliott, W.P., 1972. The effect of rainfall on the wind in the surface layer. Boundary-Layer Meteorology, 3(2), pp.146-151.

Chen, S.S., Zhao, W., Donelan, M.A., Price, J.F. and Walsh, E.J., 2007. The CBLAST-Hurricane program and the next-generation fully coupled atmosphere–wave–ocean models for hurricane research and prediction. Bulletin of the American Meteorological Society, 88(3), pp.311-317.

Chen, S.S., Zhao, W., Donelan, M.A. and Tolman, H.L., 2013. Directional wind–wave coupling in fully coupled atmosphere–wave–ocean models: Results from CBLAST-Hurricane. Journal of the Atmospheric Sciences, 70(10), pp.3198-3215.

Clayson, C.A. and Kantha, L.H., 1999. Turbulent kinetic energy and its dissipation rate in the equatorial mixed layer. Journal of physical oceanography, 29(9), pp.2146-2166.

Donelan, M.A., Haus, B.K., Reul, N., Plant, W.J., Stiassnie, M., Graber, H.C., Brown, O.B. and Saltzman, E.S., 2004. On the limiting aerodynamic roughness of the ocean in very strong winds. Geophysical Research Letters, 31(18), L18306.

Emanuel, K.A., 1995. Sensitivity of tropical cyclones to surface exchange coefficients and a revised steady-state model incorporating eye dynamics. Journal of the Atmospheric Sciences, 52(22), pp.3969-3976.

Fairall, C.W., Kepert, J.D. and Holland, G.J., 1994. The effect of sea spray on surface energy transports over the ocean. Global Atmos. Ocean Syst, 2(2-3), pp.121-142.

Fairall, C.W., Bradley, E.F., Rogers, D.P., Edson, J.B. and Young, G.S., 1996. Bulk parameterization of air-sea fluxes for tropical ocean-global atmosphere coupled-ocean atmosphere response experiment. Journal of Geophysical Research: Oceans, 101(C2), pp.3747-3764.

Fu, X., Li, H.N. and Yi, T.H., 2015. Research on motion of wind-driven rain and rain load acting on transmission tower. Journal of Wind Engineering and Industrial Aerodynamics, 139, pp.27-36.

Garratt, J.R., 1977. Review of drag coefficients over oceans and continents. Monthly weather review, 105(7), pp.915-929.

Georgiou, P.N., 1986. Design Wind Speeds in Tropical Cyclone-prone Regions. PhD Thesis University of Western Ontario, London, Ontario, Canada.

Groisman, P.Y., Karl, T.R., Easterling, D.R., Knight, R.W., Jamason, P.F., Hennessy, K.J., Suppiah, R., Page, C.M., Wibig, J., Fortuniak, K. and Razuvaev, V.N., 1999. Changes in the probability of heavy precipitation: important indicators of climatic change. In Weather and Climate Extremes (pp. 243-283). Springer Netherlands.

Guo, J.C., Urbonas, B. and Stewart, K., 2001. Rain catch under wind and vegetal cover effects. Journal of Hydrologic Engineering, 6(1), pp.29-33.

501 Holland, G.J., Belanger, J.I. and Fritz, A., 2010. A revised model for radial profiles of hurricane winds. Monthly
502 Weather Review, 138(12), pp.4393-4401.

503 Holthuijsen, L.H., Powell, M.D. and Pietrzak, J.D., 2012. Wind and waves in extreme hurricanes. Journal of
504 Geophysical Research: Oceans, 117, C09003.

505 Houk, D. and Green, T., 1976. A note on surface waves due to rain. Journal of Geophysical Research, 81(24), pp.4482-
506 4484.

507 Houze Jr, R.A., Cetrone, J., Brodzik, S.R., Chen, S.S., Zhao, W., Lee, W.C., Moore, J.A., Stossmeister, G.J., Bell,
508 M.M. and Rogers, R.F., 2006. The hurricane rainband and intensity change experiment: Observations and
509 modeling of Hurricanes Katrina, Ophelia, and Rita. Bulletin of the American Meteorological Society, 87(11),
510 pp.1503-1521.

511 Huang, C.H., 2012. Modification of the Charnock wind stress formula to include the effects of free convection and
512 swell. In Advanced Methods for Practical Applications in Fluid Mechanics. InTech, pp.47-71.

513 Huffman, G.J., Adler, R.F., Bolvin, D.T. and Nelkin, E.J., 2010. The TRMM multi-satellite precipitation analysis
514 (TMPA). In Satellite rainfall applications for surface hydrology (pp. 3-22). Springer Netherlands.

515 Jarosz, E., Mitchell, D.A., Wang, D.W. and Teague, W.J., 2007. Bottom-up determination of air-sea momentum
516 exchange under a major tropical cyclone. Science, 315(5819), pp.1707-1709.

517 Kaplan, J. and DeMaria, M., 1995. A simple empirical model for predicting the decay of tropical cyclone winds after
518 landfall. Journal of applied meteorology, 34(11), pp.2499-2512.

519 Kumar, R.R., Kumar, B.P. and Subrahamanyam, D.B., 2009. Parameterization of rain induced surface roughness and
520 its validation study using a third generation wave model. Ocean Science Journal, 44(3), pp.125-143.

521 Kummerow, C., Barnes, W., Kozu, T., Shiue, J. and Simpson, J., 1998. The tropical rainfall measuring mission
522 (TRMM) sensor package. Journal of atmospheric and oceanic technology, 15(3), pp.809-817.

523 Landsea, C.W., 2000. Climate variability of tropical cyclones: past, present and future. Storms. Routledge, New York,
524 pp.220-241.

525 Langousis, A. and Veneziano, D., 2009a. Theoretical model of rainfall in tropical cyclones for the assessment of long-
526 term risk. Journal of Geophysical Research: Atmospheres, 114, D02106.

527 Langousis, A. and Veneziano, D., 2009b. Long-term rainfall risk from tropical cyclones in coastal areas. Water
528 resources research, 45, W11430.

529 Li, Q. and Wang, Y., 2012. Formation and quasi-periodic behavior of outer spiral rainbands in a numerically simulated
530 tropical cyclone. Journal of the Atmospheric Sciences, 69(3), pp.997-1020.

531 Lin, N., Smith, J.A., Villarini, G., Marchok, T.P. and Baeck, M.L., 2010. Modeling extreme rainfall, winds, and surge
532 from Hurricane Isabel (2003). Weather and Forecasting, 25(5), pp.1342-1361.

533 Lonfat, M., Marks Jr, F.D. and Chen, S.S., 2004. Precipitation distribution in tropical cyclones using the Tropical
534 Rainfall Measuring Mission (TRMM) microwave imager: A global perspective. Monthly Weather
535 Review, 132(7), pp.1645-1660.

536 Lonfat, M., Rogers, R., Marchok, T. and Marks Jr, F.D., 2007. A parametric model for predicting hurricane
537 rainfall. Monthly Weather Review, 135(9), pp.3086-3097.

538 Meng, Y., Matsui, M. and Hibi, K., 1995. An analytical model for simulation of the wind field in a typhoon boundary
539 layer. Journal of Wind Engineering and Industrial Aerodynamics, 56(2-3), pp.291-310.

Molinari, J., Moore, P.K., Idone, V.P., Henderson, R.W. and Saljoughy, A.B., 1994. Cloud-to-ground lightning in Hurricane Andrew. Journal of Geophysical Research: Atmospheres, 99(D8), pp.16665-16676.

Powell, M.D., 1990. Boundary layer structure and dynamics in outer hurricane rainbands. Part I: Mesoscale rainfall and kinematic structure. Monthly Weather Review, 118(4), pp.891-917.

Powell, M.D., Vickery, P.J. and Reinhold, T.A., 2003. Reduced drag coefficient for high wind speeds in tropical cyclones. Nature, 422(6929), pp.279-283.

Rappaport, E.N., 2000. Loss of life in the United States associated with recent Atlantic tropical cyclones. Bulletin of the American Meteorological Society, 81(9), pp.2065-2073.

Ricciardulli, L. and Wentz, F.J., 2015. A scatterometer geophysical model function for climate-quality winds: QuikSCAT Ku-2011. Journal of Atmospheric and Oceanic Technology, 32(10), pp.1829-1846.

Samsury, C.E. and Zipser, E.J., 1995. Secondary wind maxima in hurricanes: Airflow and relationship to rainbands. Monthly weather review, 123(12), pp.3502-3517.

Shu, Z.R., Li, Q.S., He, Y.C. and Chan, P.W., 2017. Vertical wind profiles for typhoon, monsoon and thunderstorm winds. Journal of Wind Engineering and Industrial Aerodynamics, 168, pp.190-199.

Sitkowski, M., Kossin, J.P. and Rozoff, C.M., 2011. Intensity and structure changes during hurricane eyewall replacement cycles. Monthly Weather Review, 139(12), pp.3829-3847.

Smith, R.K., 1968. The surface boundary layer of a hurricane. Tellus, 20(3), pp.473-484.

Snaiki, R. and Wu, T., 2017a. Modeling tropical cyclone boundary layer: Height-resolving pressure and wind fields. Journal of Wind Engineering and Industrial Aerodynamics, 170, pp.18-27.

Snaiki, R. and Wu, T., 2017b. A linear height-resolving wind field model for tropical cyclone boundary layer. Journal of Wind Engineering and Industrial Aerodynamics, 171, pp.248-260.

Snaiki, R. and Wu, T., 2017c. Dynamic Interaction of Wind and Rain Fields in the Boundary Layer of a Tropical Cyclone. Proceedings of Engineering Mechanics Institute Conference 2017 (EMI 2017), May, 2017, San Diego, CA, USA.

Taylor, G.I., 1916. Skin friction of the wind on the earth's surface. Proceedings of the Royal Society of London. Series A, Containing Papers of a Mathematical and Physical Character, 92(637), pp.196-199.

Trenberth, K.E., Davis, C.A. and Fasullo, J., 2007. Water and energy budgets of hurricanes: Case studies of Ivan and Katrina. Journal of Geophysical Research: Atmospheres, 112(D23106).

Tse, K.T., Li, S.W., Chan, P.W., Mok, H.Y. and Weerasuriya, A.U., 2013. Wind profile observations in tropical cyclone events using wind-profilers and doppler SODARs. Journal of Wind Engineering and Industrial Aerodynamics, 115, pp.93-103.

Tuleya, R.E., DeMaria, M. and Kuligowski, R.J., 2007. Evaluation of GFDL and simple statistical model rainfall forecasts for US landfalling tropical storms. Weather and forecasting, 22(1), pp.56-70.

Vickery, P.J., Wadhera, D., Powell, M.D. and Chen, Y., 2009. A hurricane boundary layer and wind field model for use in engineering applications. Journal of Applied Meteorology and Climatology, 48(2), pp.381-405.

Willoughby, H.E., Marks Jr, F.D. and Feinberg, R.J., 1984. Stationary and moving convective bands in hurricanes. Journal of the Atmospheric Sciences, 41(22), pp.3189-3211.

Willoughby, H.E., 1988. The dynamics of the tropical cyclone core. Australian Meteorological Magazine, 36, pp.183-191.

579 Wilson, P.S. and Toumi, R., 2005. A fundamental probability distribution for heavy rainfall. Geophysical Research
580 Letters, 32, L14812.

581 Wong, B. and Toumi, R., 2016. Effect of extreme ocean precipitation on sea surface elevation and storm
582 surges. Quarterly Journal of the Royal Meteorological Society, 142(699), pp.2541-2550.

583 Woolhiser, D.A. and Roldan, J., 1982. Stochastic daily precipitation models: 2. A comparison of distributions of
584 amounts. Water resources research, 18(5), pp.1461-1468.

585 Wu, J., 1973. Spray in the atmospheric surface layer: Laboratory study. Journal of Geophysical Research, 78(3),
586 pp.511-519.

587 Yu, C.K. and Tsai, C.L., 2010. Surface pressure features of landfalling typhoon rainbands and their possible
588 causes. Journal of the Atmospheric Sciences, 67(9), pp.2893-2911.

589 Zhao, D., Ma, X., Liu, B. and Xie, L., 2013. Rainfall effect on wind waves and the turbulence beneath air-sea interface.
590 Acta Oceanologica Sinica, 32(11), pp.10-20.